ADVANCED FUNCTIONAL MATERIALS
www.afm-journal.de

Enhanced Reversible Sodium-Ion Intercalation by Synergistic Coupling of Few-Layered MoS_2 and S-Doped Graphene

Ge Li, Dan Luo, Xiaolei Wang, Min Ho Seo, Sahar Hemmati, Aiping Yu, and Zhongwei Chen**

Sodium-ion batteries (SIBs) are regarded as the best alternative to lithium-ion batteries due to their low cost and similar Na^+ insertion chemistry. It is still challenging but greatly desired to design and develop novel electrode materials with high reversible capacity, long cycling life, and good rate capability toward high-performance SIBs. This work demonstrates an innovative design strategy and a development of few-layered molybdenum disulfide/sulfur-doped graphene nanosheets (MoS_2/SG) composites as the SIB anode material providing a high specific capacity of 587 mA h g^{-1} calculated based on the total composite mass and an extremely long cycling stability over 1000 cycles at a current density of 1.0 A g^{-1} with a high capacity retention of ≈85%. Systematic characterizations reveal that the outstanding performance is mainly attributed to the unique and robust composite architecture where few-layered MoS_2 and S-doped graphene are intimately bridged at the hetero-interface through a synergistic coupling effect via the covalently doped S atoms. The design strategy and mechanism understanding at the molecular level outlined here can be readily applied to other layered transition metal oxides for SIBs anode and play a key role in contributing to the development of high-performance SIBs.

1. Introduction

As one of the most reliable energy storage technologies, lithium-ion batteries (LIBs) have been broadly implemented in portable electronics, electric vehicles, and even large-scale grid energy storage.[1] The unevenly distributed lithium resources and increasing cost of lithium raw materials, however, is hardly reconcilable with the rapidly growing demand for LIBs toward automotive applications in the near future.[2] Utilizing sodium-ion (Na^+) to replace lithium-ion (Li^+) in the rocking chair battery system can effectively mitigates the lithium shortage due to the huge availability of element Na in the earth's crust and the similarity of both Li^+ and Na^+ insertion chemistries.[3] However, most electrode materials—especially the anode materials commonly employed in LIBs (e.g., graphite and silicon) cannot directly be used as sodium-based intercalation compounds.[4] The major challenge mainly involves the significantly larger radius of solvated Na^+ than that of Li^+, leading to a low capacity originated from the limited intercalating capability of host materials, and to a poor stability originated from the dramatic volume variation.[5] The increasing need for commercially available sodium-ion batteries (SIBs) demands finding novel anode materials in order to realize competitive energy, power, cycling life, and safety to LIBs.[6]

Hard carbon is currently used as SIBs anode material due to its significant porosity and short insertion distance by randomly aligning small-dimensional graphene layers,[7] while other carbonaceous materials (nanotubes,[8] nanosheets,[9] nanofibers,[10] graphene,[11] hollow carbons,[12] etc.) are also extensively explored. Although Na^+ can be moderately accommodated, limited rate capability and high irreversible capacity are often ineluctable. Moreover, these insertion compounds exhibit low initial reversible capacity of only 100–300 mA h g^{-1} with substantial fading upon cycling. Noncarbonaceous materials have also been pursued as candidates, including many intercalation compounds (e.g., $Na_2Ti_3O_7$[13] and $NaTi_2(PO_4)_3$[14]), conversion compounds (e.g., $NiCo_2O_4$,[15] Sb_2O_4,[16] and FeS_2[17]) and alloying compounds (e.g., P,[18] Sn,[19] and Sb[20]). Most of these materials exhibit high capacity due to multiple electron reactions. For example, the Sb_2O_4 thin film delivers a reversible capacity of ≈896 mA h g^{-1}, the highest capacity for SIBs anode achieved so far.[16] However, the conversion and alloying

Dr. G. Li, D. Luo, Prof. X. Wang, Dr. M. H. Seo, S. Hemmati, Prof. A. Yu, Prof. Z. Chen
Department of Chemical Engineering
University of Waterloo
200 University Avenue West, Waterloo, ON N2L 3G1, Canada
E-mail: xiaolei.wang@concordia.ca; zhwchen@uwaterloo.ca
Prof. X. Wang
Department of Chemical and Materials Engineering
Concordia University
1455 De Maisonneuve Blvd. West, Montreal, QC H3G 1M8, Canada
Dr. M. H. Seo
Hydrogen & Fuel Cell Center for Industry
Academy and Laboratories
New & Renewable Energy Research Division
Korea Institute of Energy Research (KIER)
20-41, Sinjaesaengeneogi-ro, Haseo-myeon, Buan-gun
Jellabuk-do 56332, Republic of Korea
The ORCID identification number(s) for the author(s) of this article can be found under https://doi.org/10.1002/adfm.201702562.

DOI: 10.1002/adfm.201702562

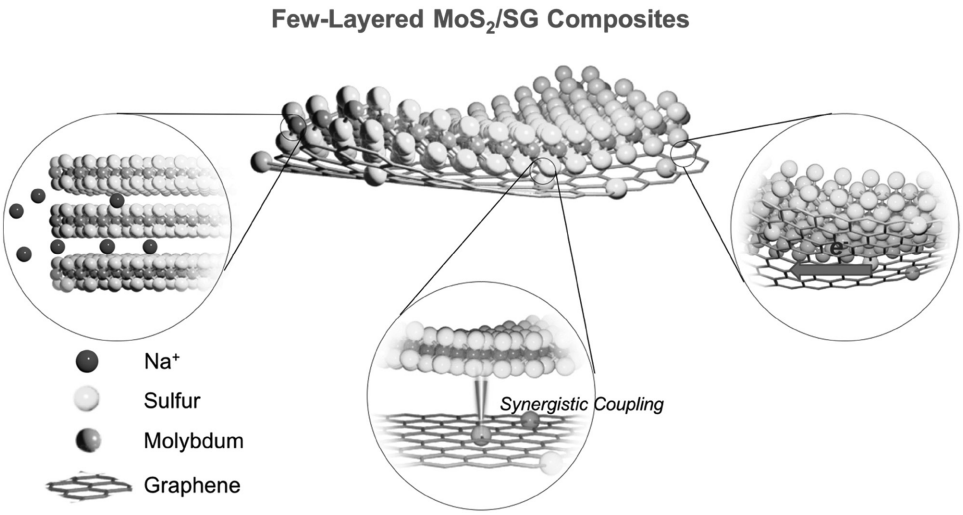

Scheme 1. The schematic of few-layered MoS_2/S-doped graphene composites with unique microstructure originated from the synergistic coupling effect. The open framework of few layered MoS_2 is capable of reversibly store large amount of Na^+, while the highly conductive graphene facilitates electron transfer. The intimate contact between the two components ensures a robust composite nanoarchitecture stemmed from the hetero-interface which provides a strong synergistic coupling via the bridging doped S atoms.

reactions are often accompanied by the huge volume variation upon charge and discharge, resulting in the collapse of microstructure and the pulverization of active material, which further hampers the capacity and cycling stability of the SIBs anode. In this context, new design strategies to address all these issues are highly desirable for the development of SIBs anode material with high reversible capacity, fast kinetics, and long cycling stability.

In order to facilitate the reversible intercalation of large amount of Na^+, three critical features are highly required:[21] (i) abundant channels and interstitial sites large enough to accept Na^+; (ii) robust material microarchitecture that maintains the stability during Na^+ intercalation/de-intercalation; and (iii) highly conductive network for fast electrons transfer. Among various candidates, 2D layered transition metal sulfides (e.g., MoS_2, WS_2, and SnS_2) with analogous structures to graphite have shown great promise for SIBs anodes owing to their pronounced redox variability and structural peculiarities.[22] Their open framework with expanded interlayer spacing is capable of reversibly store large amount of Na^+. However, these semiconductors have unsatisfactory conductivity, and tend to restack due to their intrinsic instability and lose their original microstructure during the conversion reaction with Na^+. The most common strategy involves the combination of transition metal sulfides with carbon-based materials which provide robust scaffold to improve the kinetics and integrity.[23] For example, MoS_2/CNTs[22a,24] and MoS_2/porous carbon[25] have been developed for better reversible Na^+ storage. Although an improved cycling stability can often be achieved, may not in a long term. More importantly, the fundamental

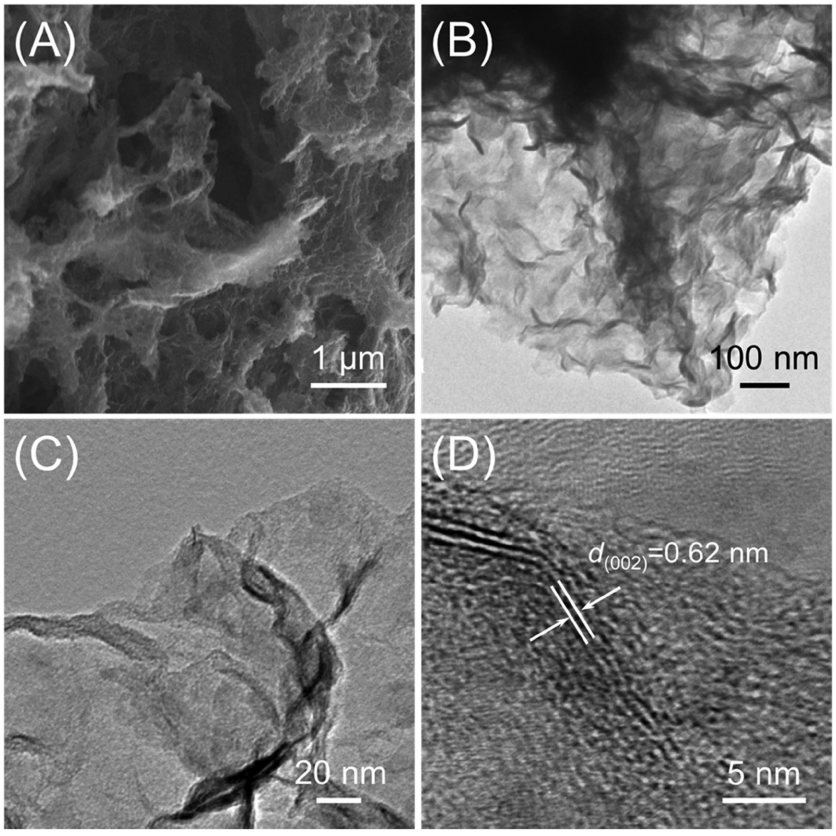

Figure 1. A) SEM and B) TEM images of as-synthesized MoS_2/SG composites; C) High-magnification TEM image of the edge area of MoS_2/SG composites; and D) High-resolution TEM image of the edge area of MoS_2 plane in the as-synthesized MoS_2/SG composites.

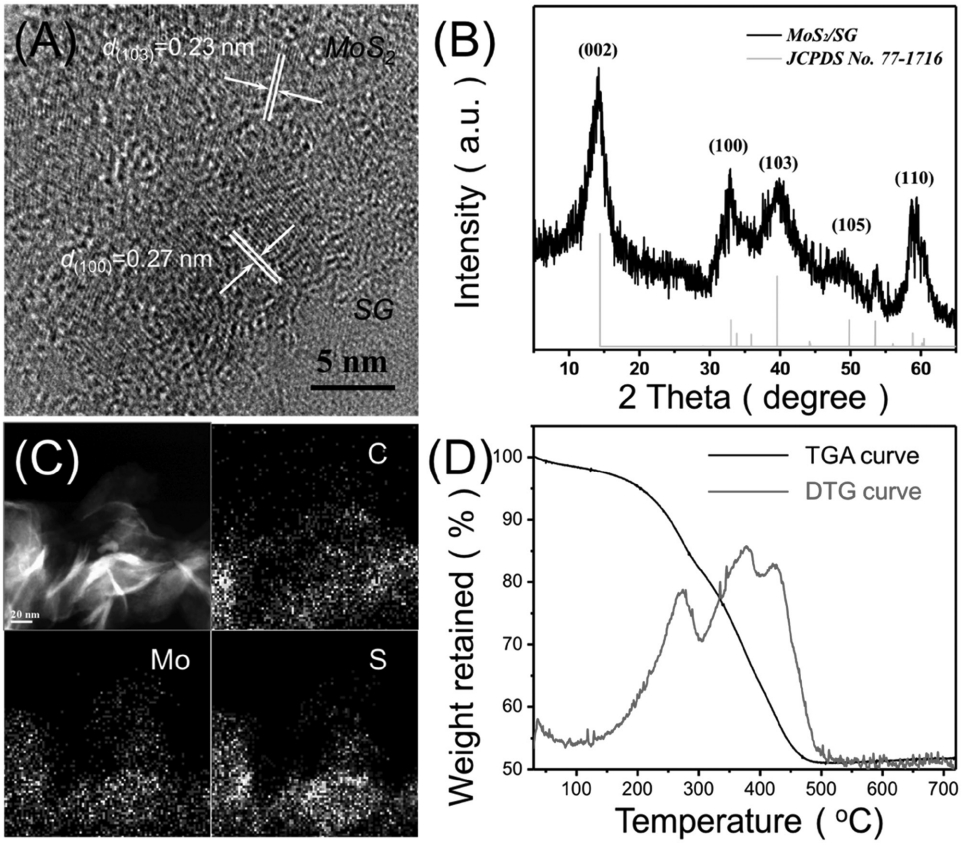

Figure 2. A) High-resolution TEM image and B) XRD pattern of as-synthesized MoS_2/SG composites; C) Elemental mapping of as-synthesized MoS_2/SG composites showing the distribution of MoS_2 and SG (up-left: spectrum image scanning, up-right: C-K mapping, bottom-left: Mo-K mapping, bottom-right: S-K mapping); and D) TGA and corresponding DTG curve of as-synthesized MoS_2/SG composites.

understanding of the interaction mechanism between the carbon materials and transition metal sulfides is still unclear at the molecular level. Therefore, the efficient design of transition metal sulfide-based composite materials for improving Na^+ storage is still greatly challenging.

Herein, we demonstrate an innovative design strategy to realize enhanced reversible Na^+ intercalation by synergistically coupling few-layered transition metal sulfides and graphene sheets through the covalently doped S atoms. As illustrated in **Scheme 1**, such a novel design not only maintains the open framework of the 2D few-layered transition metal sulfides with excellent Na^+ storage ability and high electronic conductivity of graphene, but also provides a unique robust microstructure where few-layered transition metal sulfide is firmly anchored to the graphene sheets. We find that this anchoring effect is mainly stemmed from the hetero-interface between the two components which provides synergistic coupling via the bridging doped S atoms and plays a key role in contributing to the outstanding electrochemical stability upon cycling and improved kinetics. MoS_2 is chosen as a model transition metal sulfide, and the MoS_2/S-doped graphene (MoS_2/SG) composite material undergoes a reversible insertion and conversion-type reaction with Na^+, exhibiting a high specific capacity of 587 mA h g^{-1} based on the total mass of the composites at a current density of 100 mA g^{-1} and an extremely long cycling life of over 1000 cycles at a current of 1.0 A g^{-1} with a capacity retention of ≈85%. This novel design strategy and mechanism understanding at molecular level hold great promise for the development of high-performance SIBs toward broad applications in the future.

2. Results and Discussion

2.1. Morphology of as-Synthesized MoS_2/SG

The MoS_2/SG composite material was synthesized by a facile one-pot solvothermal reaction followed by an annealing process. Element sulfur was used as precursor not only reacting with Mo precursor forming MoS_2 nanosheets grown on the graphene sheets but also functionalizing the graphene sheets in the form of covalently S-doping (Figure S1, Supporting Information), which has been reported in our previous work.[26] The morphology of the composites can be revealed by scanning electron microscopy (SEM) and transmission electron microscopy (TEM). **Figure 1**A shows a representative SEM image of as-synthesized MoS_2/SG composites, where 2D and large-piece sheet-like morphology can be found with rough and rugged surface, suggesting the in situ formation of MoS_2 on graphene nanosheets. Figure 1B displays a representative TEM image of a small piece of as-synthesized MoS_2/SG composites, where only 2D sheet-like morphology can be found without

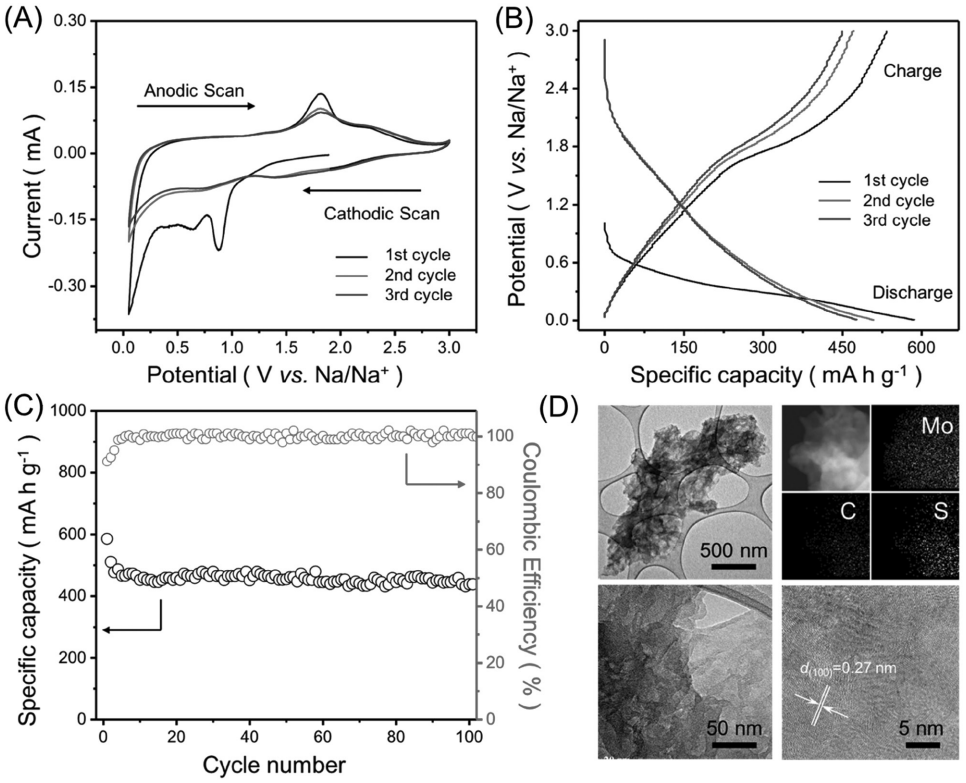

Figure 3. A) CV curves of as-synthesized MoS_2/SG composite electrode at a scan rate of 0.2 mV s^{-1} in a voltage window of 3.0–0.005 V for the first three cycles; B) Galvanostatic charge–discharge curves of as-synthesized MoS_2/SG composite electrode at a current density of 100 mA g^{-1} for the first three cycles; C) Corresponding cycling performance as well as Coulombic efficiency for 100 cycles; and D) The morphology, composition, and crystallinity of MoS_2/SG composites after cycling.

any spherical or flower-like MoS_2 that is often observed from hydrothermal synthesis.[27] Such phenomenon also suggests that this unique synthesis enables a quasiepitaxial growth of MoS_2 along the 2D graphene sheets and renders a different evolution process of MoS_2.[28] Interestingly, high-magnification TEM image in Figure 1C reveals that the MoS_2/SG composites are semitransparent, indicating both MoS_2 and graphene only possess a few layers, without severe restacking of graphene sheets and agglomeration of MoS_2 nanosheets. This observation is also confirmed by high-resolution TEM (HRTEM) image (Figure 1D), where only less than ten layers stacking can be obtained (Figure S2, Supporting Information) with the interlayer $d_{(002)}$-spacing of 0.62 nm which is consistent with the features of bulk MoS_2 and other reports.[29]

2.2. Structure and Composition of as-Synthesized MoS_2/SG

The highly crystalline feature of MoS_2 in the MoS_2/SG composites is also revealed by HRTEM image shown in **Figure 2**A, where clear lattice fringe can be observed. The continuous and periodic arrangement of the lattice fringe with some curvature not only implies that few-layered MoS_2 is single-crystal with a large domain size, but also demonstrates the high flexibility of MoS_2 by intimately anchoring onto the SG sheets. The spacing of the lattice plane is measured to be 0.27 and 0.23 nm, which corresponds to the (100) and (103) plane of the hexagonal arrangement, respectively. The crystal structure of MoS_2 in the MoS_2/SG composites is also confirmed by the X-ray diffraction (XRD) pattern (Figure 2B), which can be attributed to the P63/mmc space group (JCPDS No. 77-1716).[30] Figure 2C displays the energy-dispersive X-ray spectroscopic images of as-synthesized MoS_2/SG composites. The element mapping result indicates the existence of element C, Mo, and S, suggesting that MoS_2 forms on the graphene sheets. It can be observed that element Mo and S are homogeneously distributed along with element C, indicating the single-crystal MoS_2 nanosheets are grown intimately onto the SG sheets, which is consistent with the HRTEM observation. Figure 2D shows the thermogravimetric analysis (TGA) result of the MoS_2/SG composites. The initial mass loss of ≈5% below 200 °C is mainly due to the evaporation of surface adsorbed moisture, while the continuous weight loss between 200 and 500 °C can be attributed to the decomposition of the composite material. According to the derivative thermogravimetric (DTG) curve with three peaks, this process mainly involves three reactions. The two peaks centered at around 270 and 380 °C represent the decomposition and oxidation process of MoS_2 to MoO_3. The SG is burnt out between 400 and 450 °C that is reflected by the third peak centered at around 425 °C. Based on the TGA result, the MoS_2 is estimated to be 59.13% in the MoS_2/SG composites, which is comparable to many MoS_2-based composites for battery applications.[22a,23a]

2.3. Electrochemical Properties of MoS_2/SG Composite Electrode

The electrochemical property of as-synthesized MoS_2/SG composites was qualitatively evaluated by cyclic voltammetry technique, where the MoS_2/SG composite electrode was assembled into a CR2032 coin-typed cell with sodium foil as the counter electrode and 1.0 M sodium hexafluorophosphate in ethylene carbonate/diethyl carbonate ($NaPF_6$ in EC/DEC, v/v = 1:1) as the electrolyte. **Figure 3**A displays the representative cyclic voltammetric (CV) curves of as-synthesized MoS_2/SG composites for the first three cycles at a scan rate of 0.2 mV s^{-1} in the voltage window of 3.0–0.005 V (vs Li/Li^+). Generally, the reduction of MoS_2 can be described by two steps: (i) the insertion of Na^+ into MoS_2 interlayers, and (ii) the conversion of MoS_2 to Mo accompanied by the formation of Na_2S.[31] For the initial cathodic scan, a major peak and a small but broader peak can be observed at 0.88 and 0.65 V, respectively, along with a sharp tail below 0.4 V. The peaks at above 0.4 V can be attributed to the reversible insertion of Na^+ into MoS_2/SG interlayers and the irreversible formation of the solid-electrolyte interface (SEI) layer, during which the MoS_2 maintains its crystal structure at the beginning but is slightly distorted as more Na^+ are inserted to expand the interlayers. The sharp tail can be associated with the decomposition of MoS_2 forming metallic Mo nanograins embedded in an amorphous Na_2S matrix by the reaction between Na^+ and MoS_2.[27a] For the initial anodic scan, a very tiny bump at 1.31 V, a major peak at 1.81 V, and a broad peak at 2.30 V can be found, which corresponds to the whole process of the Mo oxidation, the MoS_2 reconstruction and the Na^+ deinsertion.[32] For the subsequent cycles, the cathodic peaks disappear, while only small and broad bumps between 3.0 and 0.4 V and shrunk tail at below 0.4 V can be observed and they are almost overlapped, indicating a highly reversible Na^+ storage process and excellent stability of the MoS_2/SG composites.

The electrochemical behavior of MoS_2/SG is also observed from the galvanostatic charging–discharging curves shown in Figure 3B. The initial discharging curve possesses a long tail below 0.4 V and charging curves show a plateau at around 1.8 V, which is consistent with the CV observations. The MoS_2/SG composites deliver an initial specific capacity of 587 mA h g^{-1} and a recovered charge capacity of 535 mA h g^{-1} at a current density of 100 mA g^{-1} calculated based on the total mass of the MoS_2/SG composites, corresponding to a high Coulombic efficiency of ≈91.2%. Obviously, the intimate quasiepitaxial growth and large size of 2D MoS_2 on graphene nanosheets effectively avoid irreversible capacity by mitigating the formation of SEI often found in graphene materials with high surface area (Figure S3, Supporting Information). The discharge capacity gradually decreases to 510 and 481 mA h g^{-1} for the 2nd and 3rd cycles, respectively, with increased Coulombic efficiency of 92.7% and 93.6%. The MoS_2/SG composite electrode exhibits a long cycling stability. After 100 cycles, a specific discharge capacity of 439 mA h g^{-1} can be maintained, corresponding to a capacity retention of 74.8%, with a Coulombic efficiency close to 100% (Figure 3C), which further confirms that the Na^+ storage of MoS_2/SG is highly reversible. By comparison, pure MoS_2 synthesized at identical condition delivers an initial discharge capacity of 714 mA h g^{-1} but shows a dramatic capacity decay (Figure S4, Supporting Information) for only 50 cycles. The outstanding

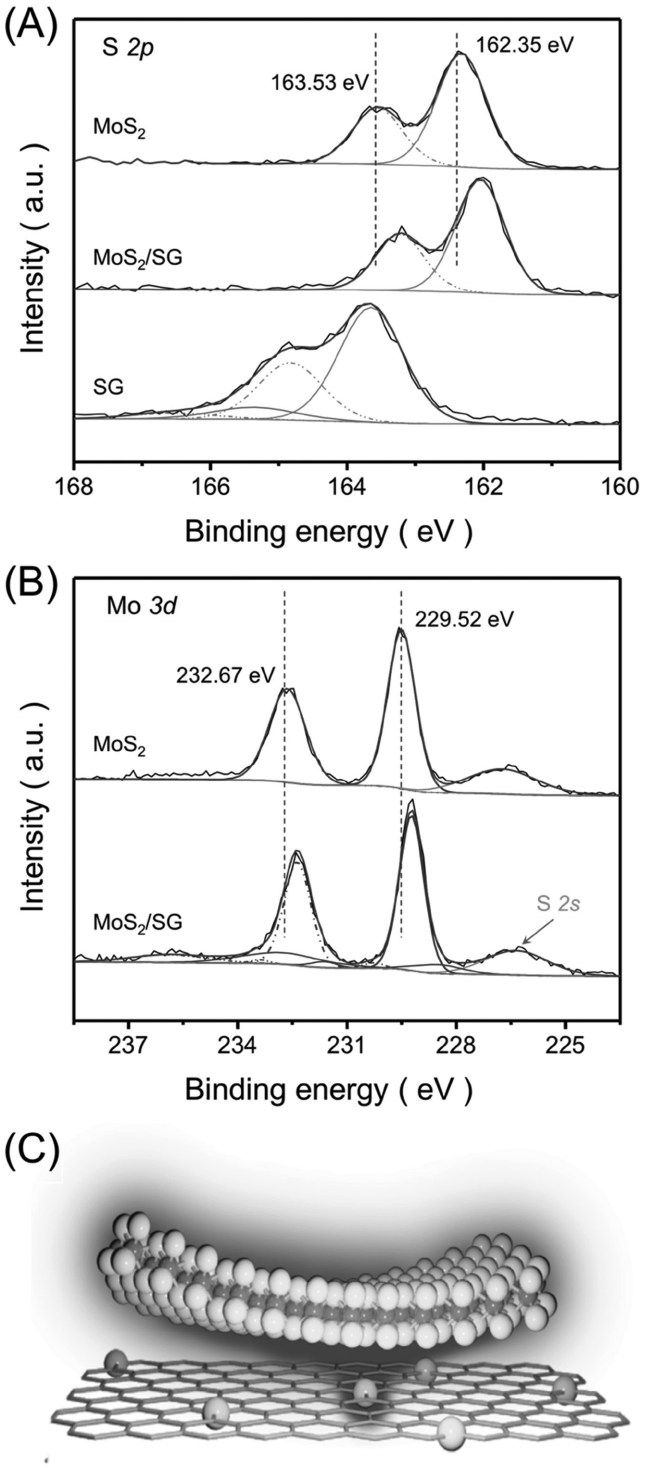

Figure 4. XPS core-leveled scan spectra of element A) S and B) Mo in pure MoS_2, pure SG, and MoS_2/SG composites, respectively; C) Schematic illustration of the electron cloud bias from SG to MoS_2 through the SG's S dopants whose electron clouds are shared with those of MoS_2 at the interface.

cycling stability is mainly due to the robust composite architecture by efficiently combining few-layered MoS_2 and S-doped graphene nanosheets. Even after repeated insertion of and conversion reaction with Na^+, few-layered MoS_2 still maintain its 2D morphology, composition, and high crystallinity without obvious agglomeration observed, and is still intimately anchored on the graphene sheets (Figure 3D).

2.4. Understanding of the Microstructure and Coupling Effect

In order to understand how such unique synergistic effect between few-layered MoS_2 and S-doped graphene provides the robust composite architecture, the interactions between few-layered MoS_2 and S-doped graphene were analyzed at molecular level using X-ray photoelectron spectroscopy (XPS) measurement (Figures S5 and S6, Supporting Information). **Figure 4**A compares the high-resolution S *2p* spectra of pure SG, pure MoS_2, and as-synthesized MoS_2/SG composites. Obviously, the SG synthesized at identical condition is successfully and covalently doped by S atoms mainly in a heterocyclic configuration, which is consistent with previous report.[33] For pure MoS_2 synthesized at identical condition, one major doublet can be found at 163.53 and 162.35 eV with a binding energy gap of 1.18 eV, which can be attributed to the S^{2-} in few-layered MoS_2. Compared to the pure MoS_2, MoS_2/SG composites also show the typical S^{2-} doublet, however, with a slight shift to the lower energy region, indicating a decreased degree of oxidation of element S in MoS_2. Interestingly, element Mo exhibits a similar variation tendency, as shown in Figure 4B, where Mo peaks in MoS_2/SG composites shift to the lower energy region when compared to those of pure MoS_2. It is evident that the electron density around MoS_2 in the MoS_2/SG composites increases. Considering the only existing two components in the composites, the electron cloud is expected to show a bias from SG to MoS_2, forming a strong electronic coupling between the two components. Generally, heterogeneous atoms (e.g., N, S, P, etc.) doping enables electron-rich graphene sheets centered at the doping atoms.[26] Note that the S *2p* peaks at relatively high energy region for pure SG disappear in the MoS_2/SG composites (Figure 4A). Obviously, the electron cloud bias from SG to MoS_2 is mainly through the SG's S dopants whose electron clouds are shared with those of S atoms in MoS_2 at the interface (Figure 4C). And this unique and strong synergistic coupling provides a robust composite structure for long-term highly reversible Na^+ storage. Raman spectra of MoS_2/SG composites (Figure S7, Supporting Information) shows two peaks located at 403.25 and 380.90 cm^{-1} with a small gap of 22.35 cm^{-1}, which are originated from the existence of MoS_2, indicating that MoS_2 possesses the few-layered nature for the efficient coupling with S-doped graphene.[34]

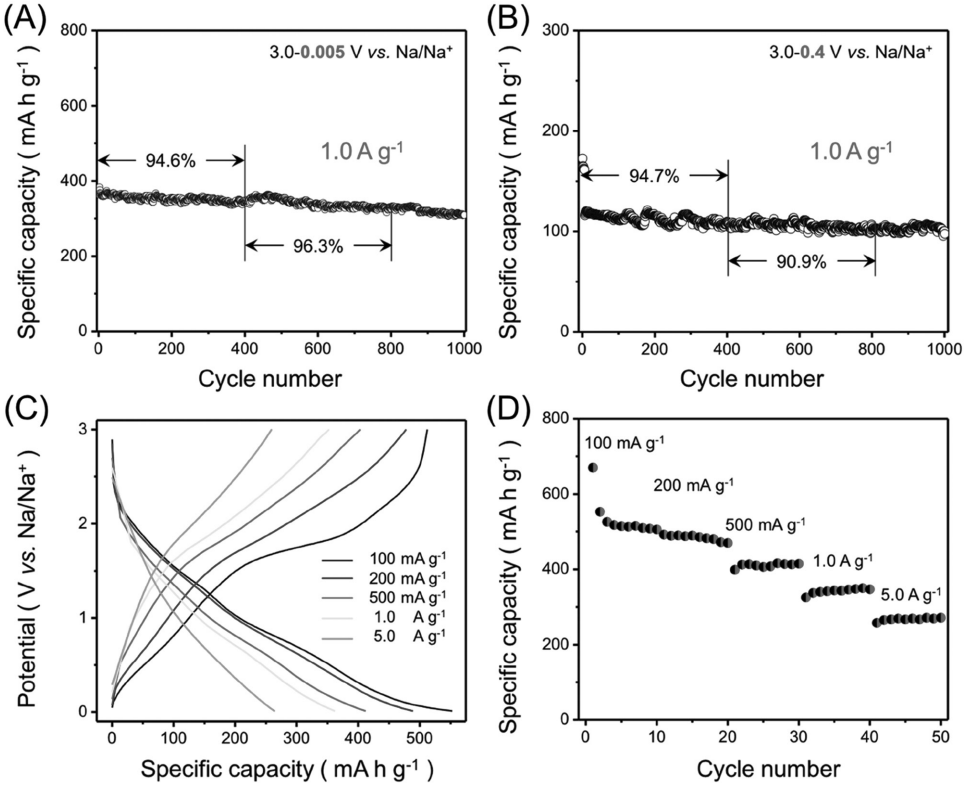

Figure 5. Long cycling performance of MoS_2/SG composite electrode at a current density of 1.0 A g^{-1} for the voltage windows of A) 3.0–0.005 V, and B) 3.0–0.4 V versus Na/Na^+; C) Galvanostatic charge–discharge profiles of MoS_2/SG composites at various current densities ranging from 100 mA g^{-1} to 5.0 A g^{-1}, and D) corresponding capacity dependence on cycle numbers.

2.5. Long Cycling and Rate Performance of MoS_2/SG Composite Electrode

The long cycling stability can be reflected from **Figure 5**A, where the composite electrode was galvanostatically charged and discharged at a current density of 1.0 A g^{-1} for over 1000 cycles. An initial and second cycle discharge capacity of 364 and 383 mA h g^{-1} obtained, respectively. A reversible discharge capacity of 309 mA h g^{-1} can be maintained, while a capacity retention of 80.7% can be achieved based on the second discharge capacity, and 84.9% based on the initial discharge capacity, corresponding to an extremely low capacity decay of only 0.019% per cycle. To further elucidate how the composite microstructure improves the stability during cycling, the MoS_2/SG composite electrode was also galvanostatically charged and discharged within a voltage window ranging from 3.0 to 0.4 V, where Na^+ insertion and deinsertion is the mainly reaction, while conversion is mostly avoided (Figure 5B). Interestingly, comparable cycling performance of MoS_2/SG composite electrode can be achieved, implying that the unique architecture of MoS_2/SG with strong coupling effect between the two components can well maintain its original structure without collapsing by the conversion reaction during deep charge/discharge process. In addition, the MoS_2/SG composites also show an outstanding rate capability for a voltage window of 3.0–0.005 V (Figure 5C). Even at a high current of 5.0 A g^{-1}, the composite electrode still delivers a reversible capacity of 264 mA h g^{-1}, corresponding to a capacity retention of ≈50% compared to the reversible capacity at 100 mA g^{-1}. The superior rate performance is mainly originated from the microstructure of the composite material where active few-layered MoS_2 is intimately attached to highly conductive SG sheets facilitating both the electron and ion transportation. Excellent rate capability of MoS_2/SG can also be achieved within the voltage window of 3.0–0.4 V (Figure S8, Supporting Information). Obviously, the kinetics is mainly determined by the interlayer spacing of MoS_2, since no obvious conversion reaction occurs during discharge process.

3. Conclusion

In summary, we have successfully developed an MoS_2/SG composite material based on a novel design strategy for SIBs application, with high specific capacity and outstanding cycling stability for efficient and reversible Na^+ storage. The superior performance is mainly attributed to the unique composite architecture where few-layered MoS_2 is intimately anchored to the SG nanosheets through a strong synergistic coupling effect via S dopants from the SG component. Such an excellent SIB anode material as well as the novel design strategy and the understanding of the coupling effect at molecular level provide great opportunities for the fabrication of high-performance SIBs for practical applications in the future.

Supporting Information

Supporting Information is available from the Wiley Online Library or from the author.

Acknowledgements

G.L. and D.L. contributed equally to this work. This research was financially supported by the National Science and Engineering Research Council of Canada (NSERC), the University of Waterloo, and the Concordia University. The authors would like to thank Dr. Carmen Andrei, Dr. Andreas Korinek, and Dr. Gianluigi Botton from Canadian Centre for Electron Microscopy at McMaster University for their great help with TEM characterizations. The authors acknowledge the assistance from Dr. Rana Sodhi for the XPS studies and analysis.

Conflict of Interest

The authors declare no conflict of interest.

Keywords

long cycling, molybdenum disulfides, sodium-ion batteries, sulfur-doped graphene, synergistic coupling effects

Received: May 12, 2017
Revised: July 7, 2017
Published online: September 4, 2017

[1] B. Dunn, H. Kamath, J.-M. Tarascon, *Science* **2011**, *334*, 928.
[2] S. Komaba, W. Murata, T. Ishikawa, N. Yabuuchi, T. Ozeki, T. Nakayama, A. Ogata, K. Gotoh, K. Fujiwara, *Adv. Funct. Mater.* **2011**, *21*, 3859.
[3] V. Palomares, P. Serras, I. Villaluenga, K. B. Hueso, J. Carretero-Gonzalez, T. Rojo, *Energy Environ. Sci.* **2012**, *5*, 5884.
[4] a) C. D. Wessells, S. V. Peddada, R. A. Huggins, Y. Cui, *Nano Lett.* **2011**, *11*, 5421; b) N. Yabuuchi, M. Kajiyama, J. Iwatate, H. Nishikawa, S. Hitomi, R. Okuyama, R. Usui, Y. Yamada, S. Komaba, *Nat. Mater.* **2012**, *11*, 512.
[5] a) V. L. Chevrier, G. Ceder, *J. Electrochem. Soc.* **2011**, *158*, A1011; b) S. P. Ong, V. L. Chevrier, G. Hautier, A. Jain, C. Moore, S. Kim, X. Ma, G. Ceder, *Energy Environ. Sci.* **2011**, *4*, 3680.
[6] S.-W. Kim, D.-H. Seo, X. Ma, G. Ceder, K. Kang, *Adv. Energy Mater.* **2012**, *2*, 710.
[7] a) D. A. Stevens, J. R. Dahn, *J. Electrochem. Soc.* **2000**, *147*, 1271; b) E. Irisarri, A. Ponrouch, M. R. Palacin, *J. Electrochem. Soc.* **2015**, *162*, A2476.
[8] J. Song, Z. Yu, M. L. Gordin, X. Li, H. Peng, D. Wang, *ACS Nano* **2015**, *9*, 11933.
[9] a) H.-G. Wang, Z. Wu, F.-L. Meng, D.-L. Ma, X.-L. Huang, L.-M. Wang, X.-B. Zhang, *ChemSusChem* **2013**, *6*, 56; b) J. Ding, H. Wang, Z. Li, A. Kohandehghan, K. Cui, Z. Xu, B. Zahiri, X. Tan, E. M. Lotfabad, B. C. Olsen, D. Mitlin, *ACS Nano* **2013**, *7*, 11004.
[10] L. Qie, W.-M. Chen, Z.-H. Wang, Q.-G. Shao, X. Li, L.-X. Yuan, X.-L. Hu, W.-X. Zhang, Y.-H. Huang, *Adv. Mater.* **2012**, *24*, 2047.
[11] X. Wang, G. Li, F. M. Hassan, J. Li, X. Fan, R. Batmaz, X. Xiao, Z. Chen, *Nano Energy* **2015**, *15*, 746.
[12] a) Y. Cao, L. Xiao, M. L. Sushko, W. Wang, B. Schwenzer, J. Xiao, Z. Nie, L. V. Saraf, Z. Yang, J. Liu, *Nano Lett.* **2012**, *12*, 3783; b) K. Tang, L. Fu, R. J. White, L. Yu, M.-M. Titirici, M. Antonietti, J. Maier, *Adv. Energy Mater.* **2012**, *2*, 873.
[13] P. Senguttuvan, G. Rousse, V. Seznec, J.-M. Tarascon, M. R. Palacín, *Chem. Mater.* **2011**, *23*, 4109.
[14] S. I. Park, I. Gocheva, S. Okada, J.-I. Yamaki, *J. Electrochem. Soc.* **2011**, *158*, A1067.
[15] R. Alcántara, M. Jaraba, P. Lavela, J. L. Tirado, *Chem. Mater.* **2002**, *14*, 2847.

[16] Q. Sun, Q.-Q. Ren, H. Li, Z.-W. Fu, *Electrochem. Commun.* **2011**, *13*, 1462.
[17] T. B. Kim, J. W. Choi, H. S. Ryu, G. B. Cho, K. W. Kim, J. H. Ahn, K. K. Cho, H. J. Ahn, *J. Power Sources* **2007**, *174*, 1275.
[18] a) J. Sun, H.-W. Lee, M. Pasta, H. Yuan, G. Zheng, Y. Sun, Y. Li, Y. Cui, *Nat. Nanotechnol.* **2015**, *10*, 980; b) J. Qian, X. Wu, Y. Cao, X. Ai, H. Yang, *Angew. Chem.* **2013**, *125*, 4731.
[19] Y. Liu, N. Zhang, L. Jiao, Z. Tao, J. Chen, *Adv. Funct. Mater.* **2015**, *25*, 214.
[20] L. Wu, X. Hu, J. Qian, F. Pei, F. Wu, R. Mao, X. Ai, H. Yang, Y. Cao, *Energy Environ. Sci.* **2014**, *7*, 323.
[21] M. D. Slater, D. Kim, E. Lee, C. S. Johnson, *Adv. Funct. Mater.* **2013**, *23*, 947.
[22] a) C. Zhu, X. Mu, P. A. van Aken, Y. Yu, J. Maier, *Angew. Chem. Int. Ed.* **2014**, *53*, 2152; b) Z. Hu, Q. Liu, S.-L. Chou, S.-X. Dou, *Adv. Mater. 29*, 1700606.
[23] a) L. David, R. Bhandavat, G. Singh, *ACS Nano* **2014**, *8*, 1759; b) M. Choi, S. K. Koppala, D. Yoon, J. Hwang, S. M. Kim, J. Kim, *J. Power Sources* **2016**, *309*, 202.
[24] a) Y. Liu, X. He, D. Hanlon, A. Harvey, J. N. Coleman, Y. Li, *ACS Nano* **2016**, *10*, 8821; b) C. Zhu, X. Mu, P. A. van Aken, J. Maier, Y. Yu, *Adv. Energy Mater.* **2015**, *5*, 1401170.
[25] S.-K. Park, J. Lee, S. Bong, B. Jang, K.-D. Seong, Y. Piao, *ACS Appl. Mater. Interfaces* **2016**, *8*, 19456.
[26] X. Wang, G. Li, M. H. Seo, F. M. Hassan, M. A. Hoque, Z. Chen, *Adv. Energy Mater.* **2015**, *5*, 1501106.
[27] a) S. H. Choi, Y. N. Ko, J.-K. Lee, Y. C. Kang, *Adv. Funct. Mater.* **2015**, *25*, 1780; b) J. Wang, C. Luo, T. Gao, A. Langrock, A. C. Mignerey, C. Wang, *Small* **2015**, *11*, 473.
[28] Y. Shi, W. Zhou, A.-Y. Lu, W. Fang, Y.-H. Lee, A. L. Hsu, S. M. Kim, K. K. Kim, H. Y. Yang, L.-J. Li, J.-C. Idrobo, J. Kong, *Nano Lett.* **2012**, *12*, 2784.
[29] H. Hwang, H. Kim, J. Cho, *Nano Lett.* **2011**, *11*, 4826.
[30] a) M.-R. Gao, M. K. Y. Chan, Y. Sun, *Nat. Commun.* **2015**, *6*, 7493; b) K. Bindumadhavan, S. K. Srivastava, S. Mahanty, *Chem. Commun.* **2013**, *49*, 1823.
[31] J. Park, J.-S. Kim, J.-W. Park, T.-H. Nam, K.-W. Kim, J.-H. Ahn, G. Wang, H.-J. Ahn, *Electrochim. Acta* **2013**, *92*, 427.
[32] Z. Hu, L. Wang, K. Zhang, J. Wang, F. Cheng, Z. Tao, J. Chen, *Angew. Chem.* **2014**, *126*, 13008.
[33] D. Higgins, M. A. Hoque, M. H. Seo, R. Wang, F. Hassan, J.-Y. Choi, M. Pritzker, A. Yu, J. Zhang, Z. Chen, *Adv. Funct. Mater.* **2014**, *24*, 4325.
[34] a) X. Geng, W. Wu, N. Li, W. Sun, J. Armstrong, A. Al-hilo, M. Brozak, J. Cui, T.-P. Chen, *Adv. Funct. Mater.* **2014**, *24*, 6123; b) Y. Li, H. Wang, L. Xie, Y. Liang, G. Hong, H. Dai, *J. Am. Chem. Soc.* **2011**, *133*, 7296.